X10 EXPANSION MICROSCOPY IN LATERAL SUPERIOR OLIVE NUCLEUS

X10 EXPANSION MICROSCOPY OPTIMIZATION FOR THE LATERAL SUPERIOR OLIVE NUCLEUS IN THE AUDITORY BRAINSTEM

By ANDREI ALEXE, B.Sc.

A Thesis Submitted to the School of Graduate Studies in Partial Fulfillment of the Requirements for the Degree Master of Science

McMaster University MASTER OF SCIENCE (2022) Hamilton, Ontario (Neuroscience)

TITLE: X10 Expansion Microscopy Optimization for the Lateral Superior Olive Nucleus in the Auditory Brainstem

AUTHOR: Andrei Alexe, B.Sc. (McMaster University)

SUPERVISOR: Dr. Deda Gillespie

NUMBER OF PAGES: x, 50

Lay Abstract

The ability to study molecules at nanometer resolution using conventional light microscopes is limited by the diffraction limit of light. Innovations in super-resolution microscopy have created techniques that permit visualization of molecules of interest past the 200-250 nm resolution limit of light. One super-resolution technique, X10 expansion microscopy, can be used alone, or in combination with other methods, to achieve resolution an order of magnitude better than that afforded by conventional light microscopy.

An immature circuit in the auditory brainstem presents interesting questions for super-resolution microscopy. As brainstem tissue differs from neocortical tissue in density and optical scattering, expansion microscopy techniques previously optimized for cortical tissue must be tested and reworked for use in the brainstem. My results show that the X10 expansion microscopy protocol can work with both adult and juvenile auditory brainstem nuclei, with no observable immunohistochemistry aberrations.

Abstract

The diffraction limit of light hinders our ability to study the interactions between biomolecules. We are limited by conventional light microscopes to a lateral resolution of approximately 200 nm. Ways exist to image at nanometer scale resolution, such as with the use of electron microscopes, but electron microscopy is not appropriate for all questions. Innovations in light microscopy over the last few decades have created a new field of imaging, known as super-resolution microscopy, where both fixed and living tissue can be imaged using multiple markers past the resolution limit of light. An array of super-resolution techniques exist, each with its own advantages and disadvantages. Here, I set out to optimize the X10 expansion microscopy technique for use in the brainstem.

Located in the auditory brainstem is the superior olivary complex, where an intricate refinement process of inhibitory connections occurs between the surrounding auditory nuclei. Of interest is the inhibitory projection from the medial nucleus of the trapezoid body to the lateral superior olive, which releases the excitatory neurotransmitter glutamate during an early developmental period. For my Master of Science research project, I have worked on optimizing the X10 expansion microscopy protocol for the auditory brainstem, with a focus on the lateral superior olive nucleus.

After optimization, I was able to achieve an expansion factor close to 10 in both adult and juvenile tissue using the X10 expansion microscopy protocol. My results exhibited no obvious abnormalities in staining in co-stained expansion microscopy experiments of vesicular neurotransmitter transporters and synaptotagmin calcium sensors in the lateral superior olive nucleus. The workflow presented here is ready for use in brainstem with secondary nanobodies or directly conjugated primary antibodies.

Acknowledgements

I would like to thank my lab members and my supervisor, Dr. Deda Gillespie, for all their guidance and help with the various questions that I had throughout my degree. Thank you, Dr. Gillespie, for always pointing me in the right direction and for teaching me how to be a scientist. Thank you, Shane Simon, for all the initial troubleshooting work that you and Raphael Chan have done for the X10 expansion microscopy protocol. I would like to also thank Dr. Katrina Choe and Dr. Paul Faure for being on my supervisory committee and for all their feedback and advice I have received during our committee meetings.

Table of Contents

List of Figures

List of Abbreviations

BSA	Bovine Serum Albumin
LSO	Lateral Superior Olive
MNTB	Medial Nucleus of the Trapezoid Body
NA	Numerical Aperture
NDS	Normal Donkey Serum
NGS	Normal Goat Serum
NMDA	N-Methyl-D-Aspartate
PAINT	Points Accumulation for Imaging in Nanoscale Topography
PBS	Phosphate Buffered Saline
SIM	Structured Illumination Microscopy
SRRF	Super-Resolution Radial Fluctuations
STED	Stimulated Emission Depletion Microscopy
STORM	Stochastic Optical Reconstruction Microscopy
Syt 1	Synaptotagmin 1
Syt 2	Synaptotagmin 2
SOC	Superior Olivary Complex
VIAAT	Vesicular Inhibitory Amino Acid Transporter
VGAT	Vesicular GABA Transporter
VCN	Ventral Cochlear Nucleus

Declaration of Academic Achievement

The optimization of the X10 expansion microscopy protocol was first started by Raphael Chan for his undergraduate thesis in Dr. Deda Gillespie's laboratory. Raphael worked together with Shane Simon, a graduate student in Dr. Deda Gillespie's laboratory. I have continued to optimize the X10 expansion microscopy protocol for the auditory brainstem by modifying protocol parameters from the original X10 expansion microscopy study. In the beginning of my Master's degree, Shane Simon collected rat brains for the experiments and assisted me in visualizing immunohistochemistry and expansion microscopy tissue at the epifluorescence microscope. I collected and sectioned all the rat brains after I was trained to perfuse rat brains and to use the epifluorescence microscope. I have performed all immunohistochemistry and expansion microscopy experiments. I imaged the tissues on the epifluorescence microscope and performed the data analysis. Shane Simon imaged the expansion microscopy data on the confocal microscope.

Impact of SARS-CoV-2 on Research

Our laboratory was closed for an extended period due to the SARS-CoV-2 pandemic. Once the lab re-opened, training opportunities and access to animal tissue were constrained. Consequently, I initially read the literature, and began learning how to immunostain and how to perform the X10 expansion microscopy protocol eight months into my Master's program. Due to delays in training, intermittent access to shared lab equipment and to brain tissue, and supply chain delays for certain reagents, I was unable to complete all of the troubleshooting as well as planned experiments. My ultimate goal in this work was to perform multiple co-stains for 4 synaptic vesicle proteins, using secondary nanobodies to reduce antibody linkage error.

In the X10 expansion microscopy protocol used here, immunostaining occurs prior to expansion. If time had permitted, I would also have tested a recently developed expansion microscopy protocol that utilizes post-expansion staining. Supply-chain delays meant however that we were unable to obtain all necessary reagents until late in my Master's program.

Introduction

Resolution Limit of Light

Light microscopy has been monumental to understanding the inner workings of our bodies, with discoveries ranging from the fundamentals of cellular biology to determining crucial steps in disease prognosis. In the past century, we have visualized the process of cell division, studied biomarkers related to various cancer types and began to understand how biomolecules in our nervous system interact. Nonetheless, we are restricted from studying mechanisms at the molecular level by the diffraction limit of light. Fundamentally, our ability to distinguish two entities as being separate in space is based on the resolution power of our imaging system.

In the late 19th century, Ernst Abbe and Lord Rayleigh formulated that the resolution of light is limited by physics (Abbe, 1873; Rayleigh, 1896). Past a certain angle, light emitted from a region of interest cannot be collected by an objective lens, resulting in the loss of valuable resolution information (Rayleigh, 1896). The attainable resolution is defined by the resolution equation, resolution $\approx 1/2 * \lambda/NA$, where λ is the wavelength of the light source and NA is the numerical aperture of the lens. The numerical aperture is defined as $NA = n*\sin\theta$, where n is the refractive index of the medium between an object and the objective lens, and the angle θ represents the farthest light rays with respect to the lens centre that can be collected. Based on the resolution equation, we can increase the resolution of an image by either decreasing the wavelength of light or by increasing the numerical aperture. Objective lenses with a numerical aperture higher than 1 are commercially available, with the highest oil-immersion objectives reaching a value of around 1.5 NA. This NA limits our resolution with visible light to about 200-250 nm in lateral resolution, which is much larger than the size of most proteins and many cellular components.

Light microscopy only utilizes the visible light region of the electromagnetic spectrum. The development of electron microscopy further improved our understanding of cellular mechanisms by taking advantage of the small electron wavelength. Although electron microscopy has been a pivotal discovery in imaging past the resolution limit of light, there is a trade-off between the improvement in resolution and the diversity of images produced. Electron microscopy cannot be used with living cells and tissue, it cannot readily be used to localize more than two proteins in the same sample, nor can it be used simultaneously for high-resolution ultrastructure and protein localization.

Super-Resolution Microscopy

The attainable resolution of a light microscope is bound by the limits of physics. However, the development of super-resolution microscopy has allowed us to circumvent the diffraction limit, while still using optical illumination. In essence, we can now visualize images at the nanometer resolution scale with fluorescence microscopy by modifying the way we illuminate the sample, collect emitted light, or analyze light emitted from fluorophores. Super-resolution microscopy techniques are divided into two different categories, deterministic super-resolution techniques and stochastic super-resolution techniques.

Deterministic Super-Resolution Microscopy

One of the first super resolution microscopy techniques was structured illumination microscopy (SIM), (M. G. L. Gustafsson, 2000; Heintzmann & Cremer, 1999). In SIM, a sample is illuminated with an excitation light of a known pattern, resulting in the formation of moiré fringes when the known patterned light is superposed with the light pattern created by the

flurophores in the sample (M. G. L. Gustafsson, 2000; Heintzmann & Cremer, 1999). In Fourier space, the moiré fringes provide high-resolution information that is lost in a conventional light microscope. Two additional rotations at specific angles of the known patterned excitation light create more moiré fringes, for a total of seven information components. Altogether, the information components contain high-resolution information for an area twice as large as the original region (M. G. L. Gustafsson, 2000; Heintzmann & Cremer, 1999). Thus, an improvement of resolution in the lateral direction by a factor of two is achieved using SIM. One limitation of the original SIM technique is that the achievable lateral resolution is about 100 nm (M. G. L. Gustafsson, 2000; Heintzmann & Cremer, 1999). Consequently, cellular components smaller than 100 nm cannot be fully resolved with SIM. Since the average size of a synaptic vesicle is approximately 40 nm (Harris & Sultan, 1995; Schikorski & Stevens, 1997) and given that the average size of a primary-secondary antibody complex is approximately 20 nm, SIM cannot be used to visualize vesicular proteins that are densely packed in a presynaptic terminal.

Stimulated emission depletion (STED) microscopy is a super-resolution microscopy technique that utilizes a STED laser beam to control whether a fluorophore is in an excited state or a relaxed state (Hell & Kroug, 1995; Hell & Wichmann, 1994; Klar et al., 2000). In STED microscopy, a sample is illuminated with an excitation laser, followed by an immediate donut-shaped surrounding STED laser. The surrounding fluorophores in the STED beam are transitioned from an excited state into a high vibrational ground state via stimulated emission and depletion to prevent fluorescence (Hell & Kroug, 1995; Hell & Wichmann, 1994; Klar et al., 2000). In STED microscopy, the appropriate STED beam wavelength must be used to transfer a fluorophore from the excitation state down to the high vibrational ground state. Since the location of the STED beam is known, the center excitation beam excites fluorophores with a high

coordinate precision. A super-resolution image in the original STED microscopy technique is created by changing the location of the donut-shaped beam of light across a sample of interest, producing an image with resolution in the range of 20-50 nm (Hell & Kroug, 1995; Hell & Wichmann, 1994; Klar et al., 2000). Although a resolution limit under 50 nm is achievable with STED microscopy, the intense light beam used during imaging can result in fluorophore photobleaching and sample damage. Additionally, a relatively small subset of commercially available fluorophores is compatible with super-resolution using STED microscopy.

Stochastic Super-Resolution Microscopy

Stochastic optical reconstruction microscopy (STORM) and photo-activated localization microscopy (PALM) are two super-resolution imaging techniques that make use of photoactivatable fluorophores to surpass the resolution limit of light. In the original STORM technique, the cyanine dye Cy5 can be switched between an active state and a dark state using different wavelengths of light (Rust et al., 2006). In STORM, a strong red laser is used to switch all fluorophores to the dark state (Rust et al., 2006). A green laser is then used to excite only a small number of fluorophores in each imaging cycle. Once activated, the fluorophores emit light when illuminated with the red laser. As a result of this photo-switching, a property of the fluorophore, only a small number of fluorophores with known coordinates are stochastically activated in one imaging cycle (Rust et al., 2006). Combining a series of image cycles that contain data from stochastically excited fluorophores can produce an image at approximately 20 nm resolution (Rust et al., 2006).

The theory in the original PALM technique is similar to STORM with respect that only a small number of stochastically photoactivatable fluorescent proteins is activated (Betzig et al.,

2006; Hess et al., 2006). Initially, a small number of inactive photoactivatable molecules is switched to the active state using a laser beam until the molecules are photobleached (Betzig et al., 2006; Hess et al., 2006). The coordinate location of each molecule can be determined due to the small number of emission events in any single image, number and since the photobleached molecules cannot emit light again. This process is repeated the until all molecules are photobleached, and the aggregate data is combined to create approximately a 20 nm super-resolution image (Betzig et al., 2006; Hess et al., 2006).

The requirement for specific fluorophores, with specific photoswitching properties, is one of the limitations of STORM/PALM. Moreover, because many individual images must be collected to reconstruct the image in super-resolution, small movement artifacts can distort the image, and reconstructing the STORM/PALM super-resolution image requires significant image processing.

An additional stochastic super-resolution microscopy technique is points accumulation for imaging in nanoscale topography (PAINT), (Sharonov & Hochstrasser, 2006). In PAINT, a super-resolution image is created when the surface of a sample is exposed to a flux of diffusible fluorescent probes that stochastically bind to the sample, and 'blink', for a brief period and subsequently detach or are photobleached (Sharonov & Hochstrasser, 2006). As the concentration and diffusion rate of fluorescent probes can be set, the probability of two fluorophores bound to a sample in proximity is low. Thus, the binding of an individual fluorophore to a sample can be detected with nanometer accuracy because of its point-spread function and signal spike (Sharonov & Hochstrasser, 2006). Multiple image cycles result in the production of approximately a 25-nm resolution image (Sharonov & Hochstrasser, 2006).

Finally, an understanding of the sources of noise present in optical images allows us to analyze multiple images and extract additional resolution. Super-resolution radial fluctuations (SRRF) is one algorithm that can be implemented as a package from ImageJ to create a super-resolution image from previously collected images (Gustafsson et al., 2016). In SRRF, pixels in one image are further divided into sub-pixels that are temporally analyzed between images. Fluctuations in a fluorophore point-spread function provide probability information that a sub-pixel contains signal, which can be separated from surrounding noise after temporal analysis of multiple images (Gustafsson et al., 2016). A resolution of 60 nm is attainable with SRRF in both fixed and live sample analysis (Gustafsson et al., 2016).

The Superior Olivary Complex

The superior olivary complex (SOC) is part of the central auditory system. The SOC is comprised of several nuclei that first integrate auditory information from both ears (Boudreau & Tsuchitani, 1968; Goldberg & Brown, 1968). The brainstem contains a right and left SOC. The lateral superior olive (LSO) nucleus and the medial nucleus of the trapezoid body (MNTB) are two nuclei located in the SOC. The LSO nucleus is involved in the process of sound localization, and it receives auditory information from the two ears. LSO cells are tonotopically organized, with cells that respond best to low-frequency sounds located in the lateral LSO limb and with cells that respond best to high-frequency sounds located in the medial LSO limb (Boudreau & Tsuchitani, 1968). Each LSO nucleus receives excitatory inputs from its respective ipsilateral ventral cochlear nucleus (VCN), and inhibitory inputs from the ipsilateral MNTB via the contralateral VCN (Boudreau & Tsuchitani, 1968; Goldberg & Brown, 1968). Inputs to the LSO

from the ipsilateral VCN are glutamatergic, while inputs to the LSO from the MNTB are GABAergic/glycinergic early in postnatal development.

Vesicular Neurotransmitter Transporters

Studies have identified that the vesicular inhibitory amino acid transporter (VIAAT) transports both GABA and glycine into synaptic vesicles (Dumoulin et al., 1999; McIntire et al., 1997; Sagné et al., 1997). VIAAT (also known as vesicular GABA transporter (VGAT)) expression has been detected in both glycinergic and GABAergic neurons across different rat brain regions, including the superior olivary complex (Chaudhry et al., 1998; Sagné et al., 1997). In glutamatergic neurons, the excitatory neurotransmitter glutamate is packaged into synaptic vesicles via two vesicular glutamate transporters (VGLUTs), known as VGLUT1 and VGLUT2 (Aihara et al., 2000; Bellocchio et al., 2000; Fremeau et al., 2001; Takamori et al., 2000). The expression of a third vesicular glutamate transporter (VGLUT3) with a related sequence to VGLUT1 and VGLUT2 was found not only in glutamatergic cell populations, but also in non-glutamatergic cells (Fremeau et al., 2002; Gras et al., 2002). In particular, VGLUT3 expression was found at classically known inhibitory neurons, including GABAergic neurons (Fremeau et al., 2002).

MNTB-LSO Projection Refinement

In adult animals, the MNTB-LSO projection is glycinergic (Bledsoe et al., 1990). During the first two postnatal weeks, multiple refinement and developmental changes occur in the MNTB-LSO projection. The major neurotransmitter released from the MNTB-LSO projection is GABA in the first few postnatal days, and a shift from GABAergic to glycinergic transmission

occurs during the first two postnatal weeks (Kotak et al., 1998). The shift from GABAergic transmission to glycinergic transmission occurs at the vesicular level, as spontaneous miniature inhibitory postsynaptic currents (mIPSCs) display decreasing levels of GABA content and increasing levels of glycine content during the first two postnatal weeks (Nabekura et al., 2004). During this period, glycine acts as a depolarizing neurotransmitter on neonatal LSO neurons as the regulation of intracellular chloride ions differs compared to adult LSO neurons (Ehrlich et al., 1999; Kandler & Friauf, 1995). In the neonatal period, chloride ions are transported into cells, and a switch in the chloride ion cotransporter occurs as neurons mature which shifts the transport of chloride ions outside a cell. The depolarizing current is mediated by glycine as the current is blocked by the application of strychnine, a glycine receptor antagonist. Further, the application of furosemide, a chloride cotransporter antagonist, can switch the depolarizing glycine potential in neonatal LSO neurons (Ehrlich et al., 1999). This coincides with the time when MNTB-LSO projections are eliminated and strengthened (Kim & Kandler, 2003). A transient expression of VGLUT3 is also present during the first two postnatal weeks in the MNTB-LSO pathway (Blaesse et al., 2005; Gillespie et al., 2005). Proper refinement of the MNTB-LSO pathway requires glutamate release, as brainstem slices of VGLUT3 $^{-/-}$ mice with loss of VGLUT3 expression show impaired refinement in the MNTB-LSO pathway (Noh et al., 2010).

Unresolved Questions in the MNTB-LSO Pathway

The neurotransmitters GABA, glycine and glutamate have been shown to be released from MNTB terminals onto LSO cells during the early developmental period. Some questions remain about whether the neurotransmitters are co-released from a single vesicular pool or co-transmitted from two distinct vesicular pools. Physiological results from the lab nevertheless

strongly support a model in which GABA/glycine and glutamate occupy and are released from different vesicle populations. In particular, release properties for GABA and glycine differ from those for glutamate (Case & Gillespie, 2011). Additionally, recordings of both spontaneous and evoked miniature events revealed that miniature events comprising both GABA or glycine and glutamate response occurred with low frequency (Alamilla and Gillespie, pers. comm.). While these physiological data point to distinct vesicle populations, to date, no microcopy data have been presented corresponding to these studies.

In the immature auditory brainstem, the calcium sensor synaptotagmin 1 (Syt1) is transiently expressed. Syt1 expression follows the spatial and the temporal expression of VGLUT3 in the auditory brainstem, and occurs during the period of glutamate release in the MNTB-LSO pathway (Cooper & Gillespie, 2011). Furthermore, during the period that Syt1 is expressed, this protein co-localizes with VGLUT3 within presumed MNTB terminals in the LSO (Cooper & Gillespie, 2011). In contrast, the predominant calcium sensor for synchronous release in the brainstem, synaptotagmin 2 (Syt2), is expressed throughout development and adulthood (Cooper & Gillespie, 2011; Fox & Sanes, 2007).

In addition to the inhibitory MNTB-LSO pathway, the LSO receives excitatory glutamatergic inputs from the ipsilateral spherical bushy cells in the VCN-LSO pathway (Cant & Casseday, 1986; Wu & Kelly, 1992). In the VCN-LSO pathway, refinement of both input number and input strength is observed during the first postnatal week (Case et al., 2011). One receptor type that the released glutamate neurotransmitter can bind to is the N-methyl-D-aspartate (NMDA) receptor. During the first postnatal week, glutamate spillover from the VCN-LSO pathway and glutamate spillover from the MNTB-LSO pathway both activate a shared NMDA receptor population (Alamilla & Gillespie, 2011). Most of the NMDA current in the first

postnatal week is caused by GluN2B-containing receptors (Case et al., 2011; Case & Gillespie, 2011). A reduction in the NMDA-mediated response was observed during the first postnatal week after the application of a GluN2B antagonist, with minimal response reduction after which is indicative of a different NMDA subunit expression after the first postnatal week (Case et al., 2011; Case & Gillespie, 2011). Changes in the expression of different voltage-gated calcium channels have also been observed in the developing LSO, with channel type contributions varying by postnatal age (Alamilla & Gillespie, 2013).

Expansion Microscopy

Expansion microscopy is a recently developed microscopy technique that can attain super-resolution imaging levels with conventional microscopes, such as epifluorescence and confocal microscopes (Chen et al., 2015). With expansion microscopy, a swellable polymer network is incorporated into a labelled tissue or specimen via a chemical anchor. Proteolytic digestion is then used to ensure that a tissue sample or a specimen expands isotropically when added to water (Chen et al., 2015). Although homogenization occurs in the tissue sample or specimen, the fluorophore position does not change due to the chemical anchor between the sample and the gel. Whereas the original expansion microscopy protocol achieved approximately a 4-fold expansion factor, newer "X10 expansion microscopy" allows for a 10-fold isotropic expansion of a sample with minimal distortion between the pre-expansion and post-expansion tissue (Truckenbrodt et al., 2018). As a result, the resolution attained is improved by a factor of 10 post-expansion to a value of approximately 25 nm using an epifluorescence microscope (Truckenbrodt et al., 2018). In theory, this 10-fold increase in the resolution limit makes possible studies involving synaptic vesicles and vesicle proteins.

For my Master's degree I have worked on optimizing the X10 expansion microscopy protocol for brainstem tissue, with a focus on the LSO nucleus. The X10 expansion microscopy protocol can be used to image GABA, glycine, and glutamate vesicular transporters to determine if co-transmission or co-release occurs at the developing MNTB-LSO projection. Further, this technique can be used to image the calcium sensors synaptotagmin-1 and synaptotagmin-2 to determine their relative proximity with respect to the vesicular neurotransmitter transporters. The X10 expansion microscopy protocol can also be used to image GluN2B-containing receptor immunoreactivity during the first postnatal week along with the NMDA receptor subunit switch after the first postnatal week. Lastly, the location of different voltage-gated calcium channels in the early developmental period can be visualized using the expansion microscopy protocol.

Methods

Tissue Collection

All experimental procedures were in accord with the guidelines set by the Canadian Council on Animal Care and approved by the McMaster University's Animal Research Ethics Board. Male and female Sprague-Dawley rats from the same litter at postnatal days 8-11 (P8-P11) were collected from the breeding colony and euthanized with sodium pentobarbital (120 mg/kg). P28/P37 rats were deeply anaesthetized with isoflurane prior to euthanasia and were used to test the X10 expansion microscopy protocol on adult brain tissue. Animals were transcardially perfused with 1X PBS, followed by cold 10% buffered formalin. Animals were perfused with approximately 1 mL of PBS/formalin per gram weight at a rate of approximately 2 mL/minute. Brains were post-fixed in 10% buffered formalin for 20-24 hours and then cryoprotected in 30% sucrose in 1X PBS. Coronal brainstem sections containing the SOC were collected at a thickness of 30 μm on a freezing microtome (Microm HM 450) and stored (1-2 days) in wells containing 1X PBS prior to immunostaining.

Immunohistochemistry

All incubation steps were performed on free-floating sections on a shaker at 4ºC for 24 ± 2 hours. Diluted serum and antibody solutions were first vortexed and centrifuged to separate supernatant liquid from aggregated proteins. Stored sections were first washed twice in a 0.5% BSA (BioShop, catalog # ALB001) 1X PBS solution for 10 minutes each. Sections were permeabilized and blocked in a solution containing 0.5% Triton X-100 (Fisher Scientific, BP151) and 5% normal serum in 0.5% BSA 1X PBS. Either 5% NDS (Jackson

ImmunoResearch, catalog # 017000121) and/or 5% NGS (Jackson ImmunoResearch, catalog # 005000121) were used based on the secondary antibody host species.

Each immunohistochemistry experiment included 'primary delete' and 'secondary delete' controls, in which the sections were not exposed to all steps of the protocol except for the primary antibody, or of the secondary antibody. Additionally, each co-stain experiment included three primary delete controls – leaving out one of, or the other, or both, primary antibodies – and three secondary delete controls – leaving out one of, or the other, or both, secondary antibodies.

Primary Antibody Step

A transfer pipette was used to remove the blocking solution. Free-floating sections were washed three times for a duration of 10 minutes each in 0.5% BSA 1X PBS after the blocking step. Free-floating sections were incubated in primary antibodies containing 5% normal serum and diluted in 0.5% BSA 1X PBS. Sections absent of primary antibodies were used as a control and incubated in the same volume of 0.5% BSA 1X PBS.

Secondary Antibody Step

Transfer pipettes were used to remove the primary antibody solution. Cross-contamination of primary antibodies was minimized by using different transfer pipettes for the experimental and control sections. Free-floating sections were washed three times for a duration of 10 minutes each in 0.5% BSA 1X PBS after the primary antibody step. Sections were then incubated in secondary antibodies diluted in 0.5% BSA 1X PBS. Sections absent of secondary antibodies were used as a control and incubated in the same volume of 0.5% BSA 1X PBS.

Tissue Mounting

Transfer pipettes were used to remove the secondary antibody solution. Cross-contamination of secondary antibodies was minimized by using different transfer pipettes for the experimental and control sections. Free-floating sections were washed three times for a duration of 10 minutes each in 0.5 % BSA 1X PBS after the secondary antibody step. Sections were then washed two times for a duration of 10 minutes each in 1X PBS. Stained sections along with primary and secondary antibody control sections were placed in a container filled with 1X PBS and transferred onto subbed slides using a fine paintbrush. Sections were air-dried on a slide rack and then mounted using Fluoromount-G (SouthernBiotech, catalog # 0100-01) mounting medium (SouthernBiotech, catalog # 0100-01) and coverslipped. Sections were let to dry for approximately 5 minutes and then sealed with CoverGrip (Biotium, catalog # 23005).

LSO Microdissection

The LSO nucleus was micro-dissected from immunostained sections with the aid of a stereo microscope. Immunostained sections were added to a petri dish containing 1X PBS and dissected using a #20 scalpel blade. The LSO was micro-dissected by contrasting the shape of the nucleus from the surrounding tissue with the aid of an external light source. Repurposed tungsten electrodes were used to transfer the micro-dissected LSO nuclei from the petri dish into a well plate. Micro-dissected LSO nuclei were stored at 4º C in 1X PBS overnight. A detailed procedure of the LSO nucleus micro-dissection is included in the appendix.

Anchoring Step

Using a modified Pasteur pipette, 1X PBS was removed from the wells containing micro-dissected LSO nuclei, where the pipette was fire polished to produce a narrower diameter tip. This provided greater suctioning control and prevented the micro-dissected sections from being taken up into the Pasteur pipette. Alternatively, micro-dissected LSO nuclei were also transferred from wells containing 1X PBS into wells containing the anchoring solution via the aid of a fine metal wire (i.e., tungsten electrode). Micro-dissected LSO nuclei were incubated in a solution containing 0.2 mg/mL Acryloyl-X in 1X PBS for 24 hours on a shaker at room temperature. A detailed procedure of the anchoring step is included in the appendix.

X10 Expansion Microscopy

The X10 expansion microscopy protocol used for micro-dissected LSO nuclei was adapted and optimized from the original protocol developed by Truckenbrodt et al., 2018. A bench protocol version along with troubleshooting information for brainstem tissue is included in the appendix.

Measurement of Expansion Factor

Length and width measurements for IHC control, gelation control, digestion control and expansion microscopy tissue were calculated by measuring the inner signal boundary around a cell using pixel number in Fiji (Schindelin et al., 2012). For each expansion microscopy protocol control, the length and width measurements of three different cells were averaged and used to as the length and width measurements for the respective controls. The length and width expansion

factor for each expansion microscopy section was measured from a single cell located in the expanded tissue.

Imaging

All immunohistochemistry and expansion microscopy images were performed on an Olympus BX51 upright epifluorescence microscope**.** An Olympus LUCPlanFL N 20X air objective (0.45 NA) was used to image all immunohistochemistry control sections, gelation control sections, digestion control sections, and several expansion microscopy sections. An Olympus UPlanSApo 20X oil objective (0.85 NA) was used to image all other expansion microscopy sections. Images were collected using a CM3-U3-50S5M-CS camera (FLIR Integrated Imaging Solutions, Inc.) and displayed using Micro-Manager 2.0 Gamma. Each expansion microscopy section was imaged under adjusted camera gain and exposure time for optimal image acquisition. All antibody titrations and X10 expansion microscopy protocol optimization experiments were imaged with constant camera gain and exposure time per experiment.

Image Analysis

All antibody titrations were visually inspected on an Olympus BX51 microscope with a 20X air objective. All X10 expansion microscopy protocol optimization experiments and all expansion microscopy images were collected as TIFF files and analyzed in Fiji.

Results

Optimized X10 Expansion Microscopy Protocol with Adult Brain Tissue

First, we asked if the expansion microscopy protocol can be used with adult brainstem tissue. To test this, I expanded adult P28 tissue using an antibody for Syt2, the calcium sensor that is expressed throughout development in the LSO. Adult LSO cell bodies were expanded with the X10 expansion microscopy protocol. An expansion factor of 9.19X lengthwise and 7.64X widthwise was achieved for a P28 LSO cell when compared to the average size of an IHC control LSO cell (Fig. 1). Both gelation and digestion controls expanded compared to the IHC control. Syt2 immunoreactivity signal retention was achieved in the gelation control, digestion control and expansion microscopy tissue of a P28 cell (Fig. 1). In general, Syt2 immunoreactivity signal intensity decreased between each control of the expansion microscopy protocol. The lowest levels of Syt2 immunoreactivity were observed in the expansion microscopy tissue (Fig. 1D). The decreased signal in the expansion microscopy tissue can be attributed to the action of proteinase K activity in the digestion incubation step, along with the decrease in fluorophore density as a tissue sample expands.

Further, Syt2 immunoreactivity signal retention was achieved in older adults in both the gelation control and digestion control of P37 cells (Fig. 2). The increase in myelination content observed in adult brain tissue did not cause any novel challenges during the X10 expansion microscopy protocol of P28 and P37 adult LSO nuclei. Imaged expansion microscopy tissue of adult LSO cells appeared similar to expansion microscopy tissue of juvenile LSO cells, and no tissue tears were observed in P28 and P37 LSO cells (data not shown).

Optimized X10 Expansion Microscopy Protocol with Juvenile Brain Tissue

Next, we asked if the expansion microscopy protocol can be used with juvenile brainstem tissue. To test this, I expanded P11 LSO cells with the optimized X10 expansion microscopy protocol. An expansion factor of 8.69X lengthwise and 7.70X widthwise was achieved for a P11 LSO cell when compared to the average size of an IHC control LSO cell (Fig. 3). Both gelation and digestion controls expanded compared to the IHC control. Analysis of VGLUT3 and VIAAT immunoreactivity signal retention was observed in the gelation control, digestion control and expansion microscopy tissue of P11 LSO synapses (Fig. 3). Similar to the adult brainstem data, both VGLUT3 and VIAAT signal intensity decreased at each subsequent control step of the expansion microscopy, with the lowest signal level observed in the expansion microscopy tissue (Fig. 3H).

We then asked if the transiently expressed VGLUT3 at the MNTB-LSO projection is in proximity with Syt1 or Syt2 during the first two postnatal weeks at the MNTB-LSO projection. Expression of VGLUT3 and Syt1 immunoreactivity in P11 tissue is observed in expansion microscopy data (Fig. 4C). The data indicate that VGLUT3 and Syt1 immunoreactivity do not show strong signal proximity due to low signal overlap in expansion microscopy tissue compared to IHC control tissue (Fig. 4). A similar observation was found for VGLUT3 and Syt2 immunoreactivity in P10 tissue, as the signals were dispersed in expansion microscopy tissue (Fig. 5).

Optimized X10 Expansion Microscopy with MNTB Tissue

To determine if the optimized expansion microscopy protocol is compatible with surrounding nuclei in the SOC, we examined signal retention in expanded P10 MNTB tissue.

Signal retention for Syt2 immunoreactivity is observed in the gelation control, digestion control and expansion microscopy tissue of P10 MTNB Calyces of Held (Fig. 6). Furthermore, an expansion factor of 9.78X was calculated for one MNTB cell when compared to IHC control cells (Fig. 6). Overall, no novel challenges were encountered during the X10 expansion microscopy experiment of MTNB tissue.

Confocal Data of VGLUT3 & VIAAT Co-Stain Expansion Microscopy

Lastly, we expanded P11 tissue and analyzed VIAAT and VGLUT3 immunoreactivity using an inverted confocal microscopy and imaged at a Nyquist sampling frequency to obtain higher resolution images compared to the previously collected VGLUT3 and VIAAT expansion data (Fig. 3). The data of VIAAT and VGLUT3 immunoreactivity display clear spatial separation in expansion microscopy tissue (Fig. 7). The confocal image displays that the VGLUT3 immunoreactivity delineates the classic shape of a cell body in the merged image (Fig. 7C). Scattered regions of high VIAAT immunoreactivity are present in the merged image along with dispersed VIAAT immunoreactivity (Fig. 7C). The collected results for VGLUT3 and VIAAT immunoreactivity are of higher quality on the confocal microscope compared to the images collected on the epifluorescence microscope. Nevertheless, the collected confocal images are not at the achievable super-resolution scale of the expansion microscopy protocol.

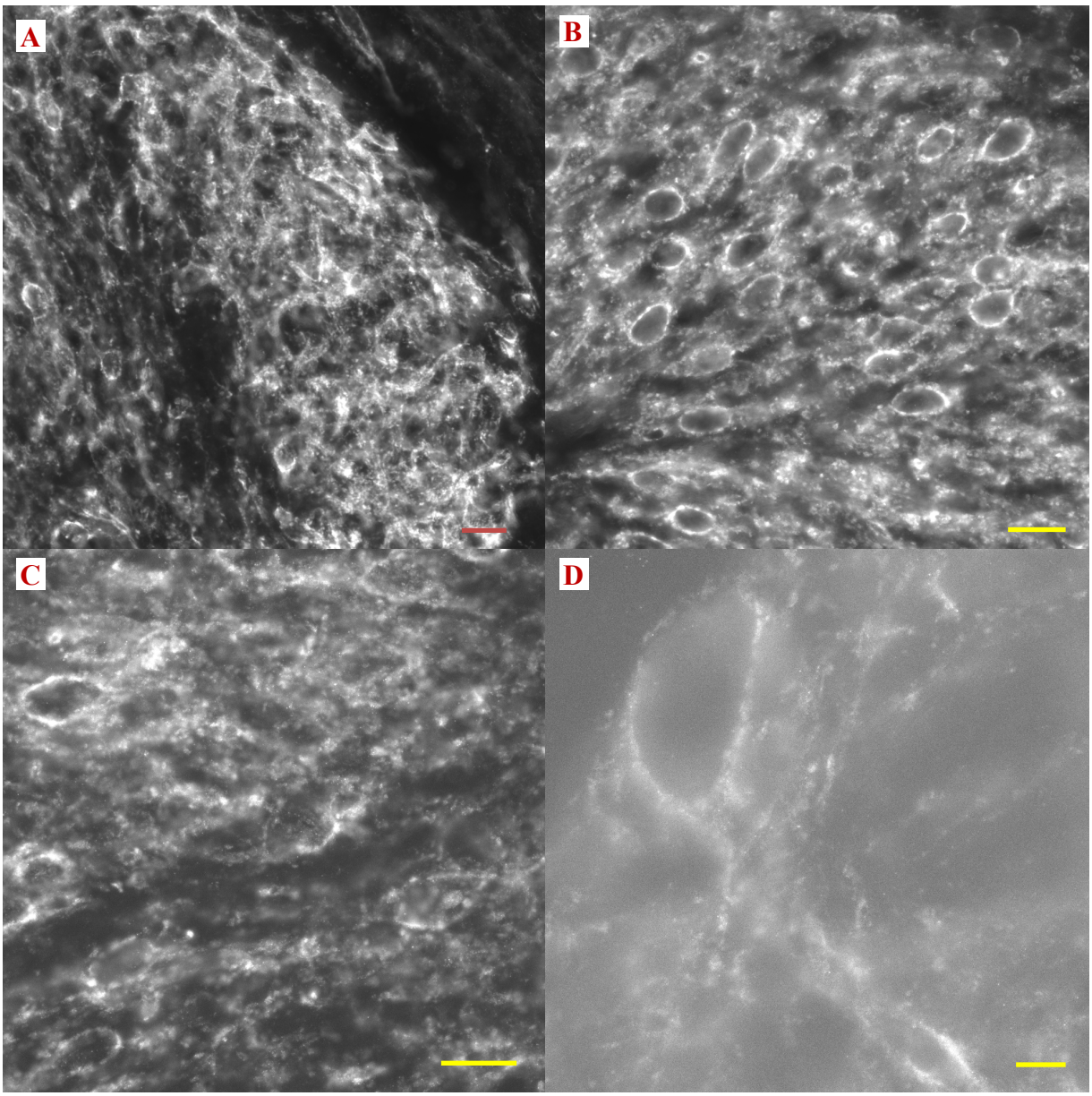

Figure 1: Raw data of P28 LSO cells in IHC control (A), gelation control (B), digestion control (C), and expansion microscopy tissue (D). Compared to IHC control, length and width expansion factors for gelation control are 1.91X and 1.80X, respectively. Compared to IHC control, length and width expansion factors for digestion control are 2.96X and 2.52X, respectively. Compared to IHC control, length and width expansion factors for expansion microscopy tissue are 9.19X and 7.64X, respectively. Images were collected with a 20X air objective (0.45 NA). Scale bar: (A) 50 µm. Estimated scale bars: (B) 60 µm; (C) 120 µm; (D) 90 µm. Estimated scale bars based on the expansion factor for the gelation, digestion and expansion microscopy data.

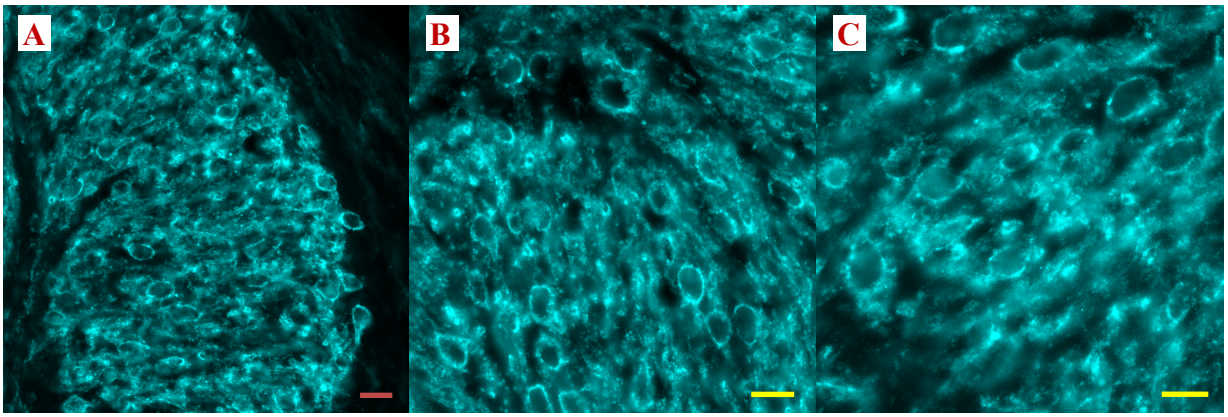

Figure 2: Overview of P37 LSO cells in IHC control (A), gelation control (B), and digestion control (C). Cyan displays Syt2 immunoreactivity visualized with Alexa Fluor 488. Images were collected on a 20X air objective (0.45 NA) and adjusted once for brightness/contrast in Fiji. Scale bar = 50 µm. Estimated scale bars: (B) = 80 µm; (C) 100 µm.

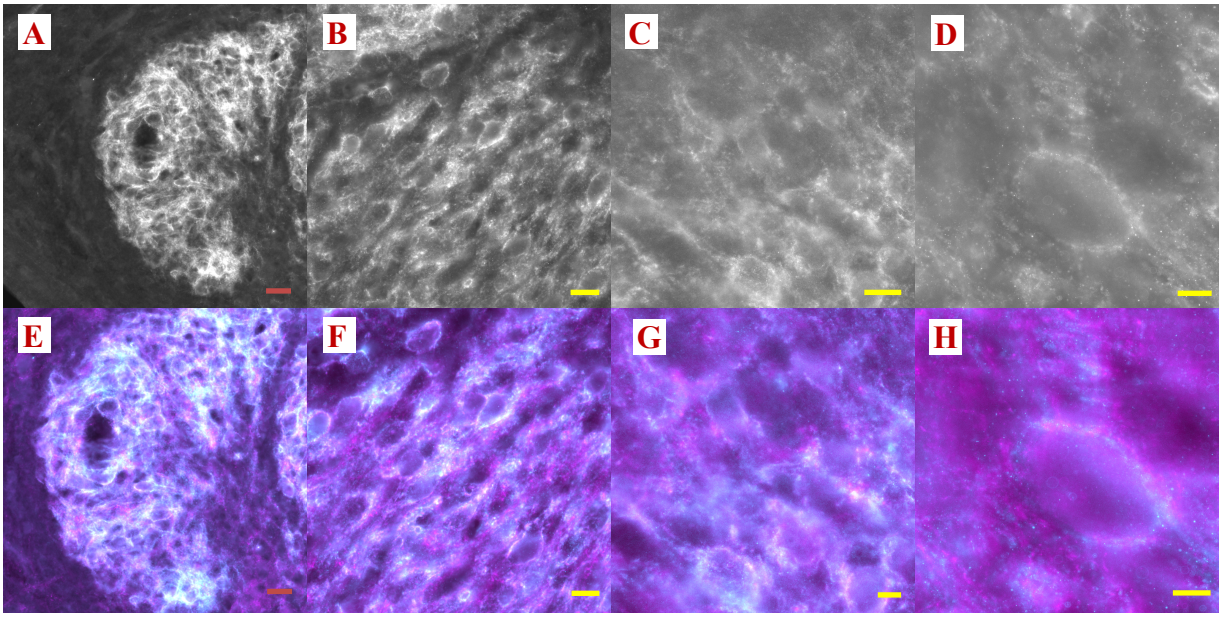

Figure 3: Raw and immunoreactivity data of P11 LSO cells in IHC control (A, E), gelation control (B, F), digestion control (C, G), and expansion microscopy tissue (D, H). A-D represents the raw data, and E-H represents the immunoreactivity representation for the same experiment. Compared to IHC control, length and width expansion factor for gelation controls are 2.14X and 1.59X, respectively. Compared to IHC control, length and width expansion factors for digestion control are 3.00X and 2.37X, respectively. Compared to IHC control, length and width expansion factors for expansion microscopy tissue are 8.69X and 7.70X, respectively. Cyan displays VGLUT3 immunoreactivity visualized with Alexa Fluor 488 and magenta displays VIAAT immunoreactivity visualized with Atto 647N. IHC, gelation and digestion control images were collected with a 20X air objective (0.45 NA). Expansion microscopy image was collected with a 20X oil objective (0.85 NA). Images E-H were adjusted once for brightness/contrast with Fiji. Scale bar: (A, E) 50 µm. Estimated scale bars: (B) 80 µm; (C) 100 µm; (D) 80 µm; (F) 40 µm; (G) 40 µm; (H) 90 µm. Estimated scale bars based on the expansion factor for the gelation, digestion and expansion microscopy data.

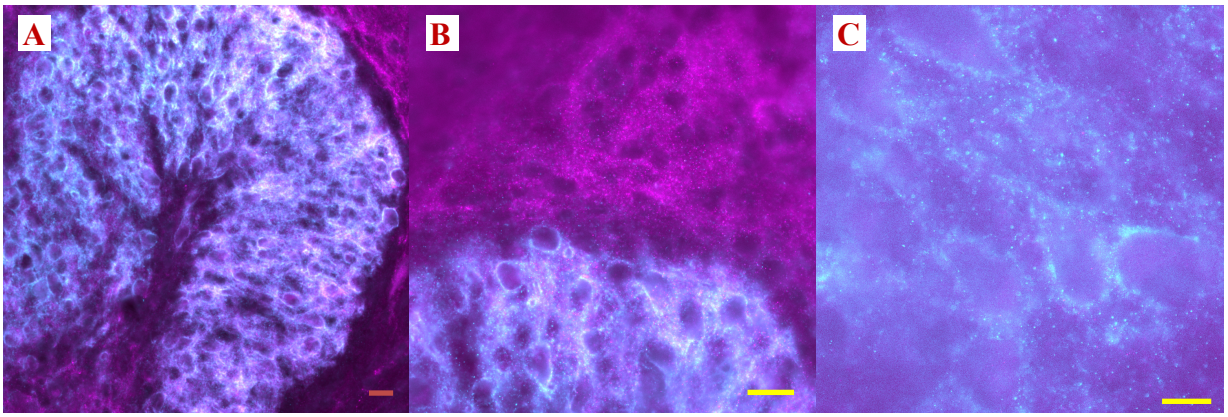

Figure 4: Overview of P11 LSO cells in IHC control (A), gelation control (B), and expansion microscopy tissue (C). Cyan displays VGLUT3 immunoreactivity visualized with Alexa Fluor 647 and magenta displays Syt1 immunoreactivity visualized with Alexa Fluor 488. IHC and gelation control images were collected with a 20X air objective (0.45 NA). Expansion microscopy image was collected with a 20X oil objective (0.85 NA). Images are adjusted once for brightness/contrast in Fiji. Scale bar = 50 µm. Estimated scale bars: (B) = 80 µm; (C) 120 µm.

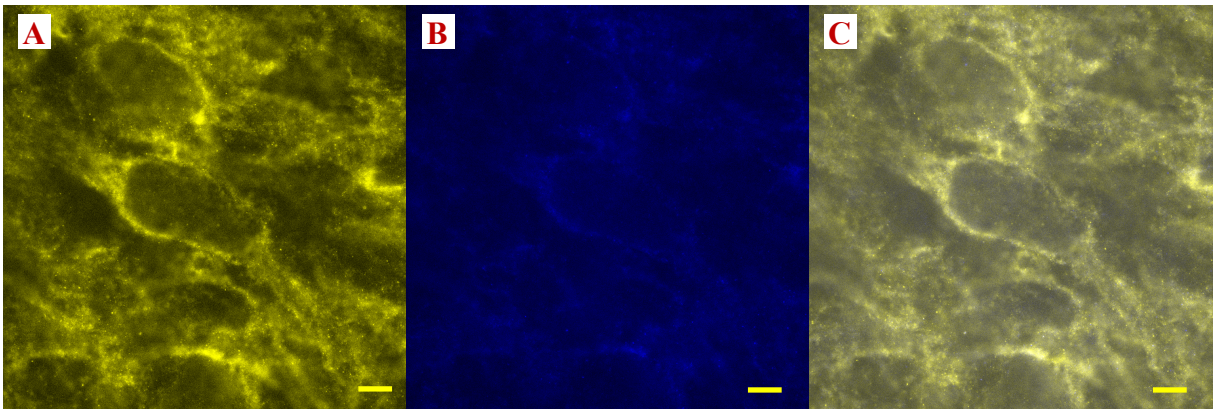

Figure 5: Overview of P10 expansion microscopy LSO cells imaged with a 20X air objective (0.45 NA). Yellow (A) displays Syt2 immunoreactivity visualized with Atto 488 and blue (B) displays VGLUT3 immunoreactivity visualized with Atto 647N. Merged Syt2 and VGLUT3 immunoreactivity (C). Images were adjusted once for brightness/contrast in Fiji. Estimated scale bar: 80 µm.

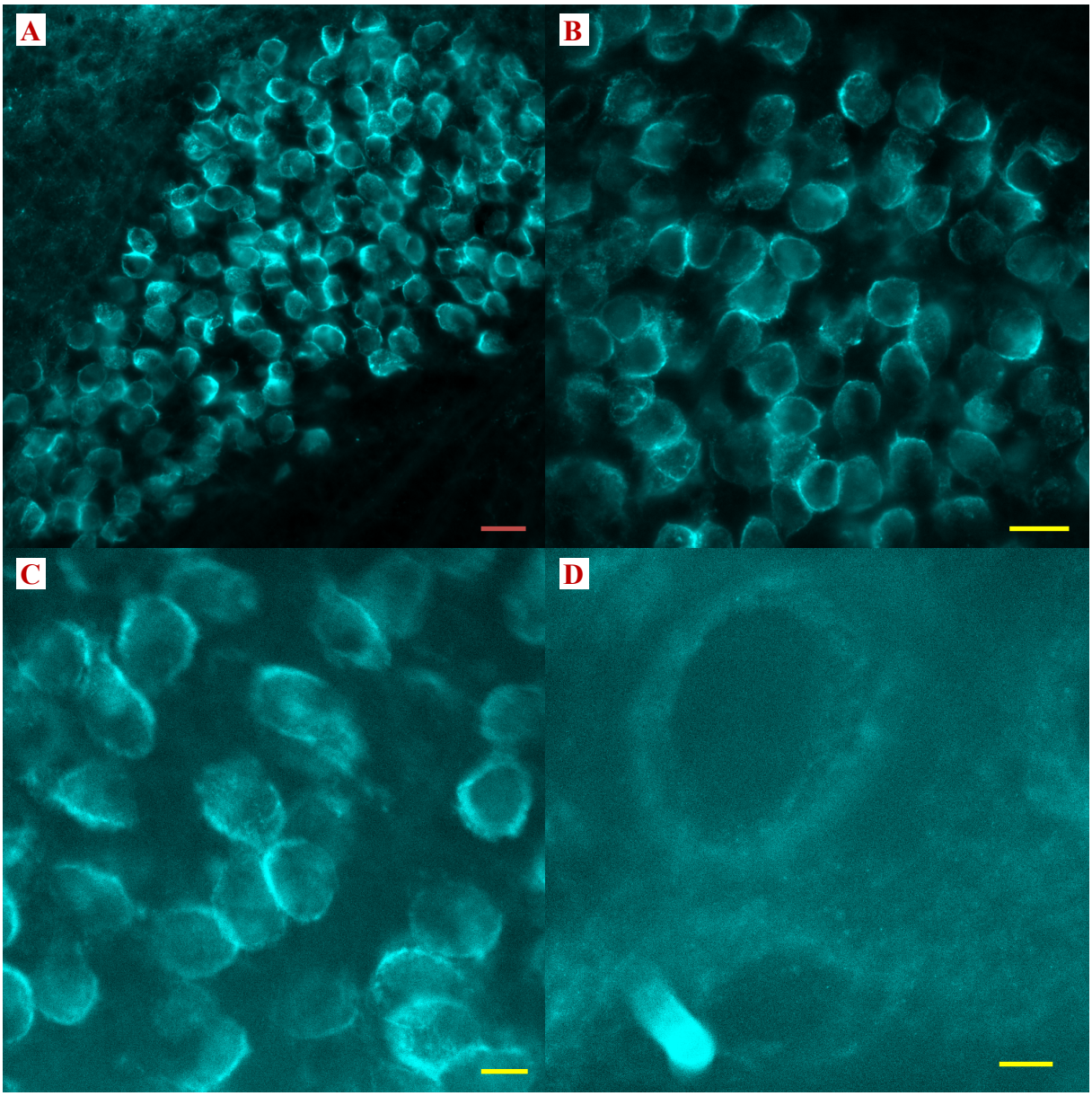

Figure 6: Overview of P10 MNTB Calyces of Held in IHC control (A), gelation control (B), digestion control (C), and expansion microscopy tissue (D). Cyan displays Syt2 immunoreactivity visualized with Alexa Fluor 488. Compared to IHC control, expansion factor for the gelation control was 2.08X and 3.37X for the digestion control. Compared to the IHC control, an expansion factor of 9.78X was calculated for the expansion microscopy tissue. Images were collected on a 20X air objective (0.45 NA) and adjusted once for brightness/contrast in Fiji. Scale bar = 60 µm. Estimated scale bars: (B) 100 µm; (C) 60 µm; (D) 100 µm. Estimated scale bars based on the expansion factor for the gelation, digestion and expansion microscopy data.

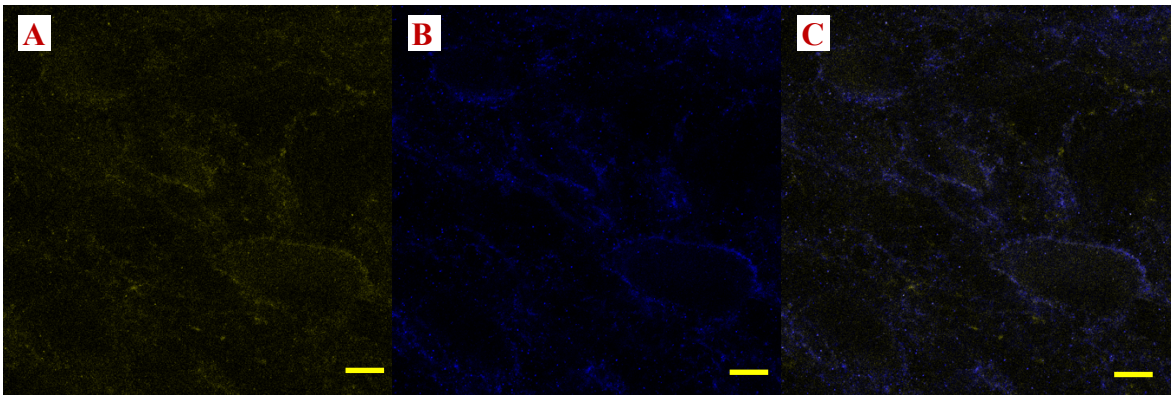

Figure 7: Single optical sections of VIAAT immunoreactivity (A), VGLUT3 immunoreactivity (B) and merged VGLUT3 and VIAAT immunoreactivity (C) in P11 expansion microscopy LSO cells. Images were collected on an inverted Nikon A1R HD25 confocal microscope with a 20X air objective (0.75 NA) at Nyquist sampling and adjusted once for brightness/contrast in Fiji. Estimated scale bar: 80 µm.

Discussion

Expansion Microscopy Shrinkage May Occur in Adult and Juvenile Tissue

Two potential explanations exist for the calculated expansion factor under X10 in the adult and juvenile expansion microscopy tissue (Figs. 1 and 3). The first reason could result from P11 and P28 expansion microscopy tissue shrinkage from the time of tissue mounting to the time of imaging. Anywhere between 4-6 expansion microscopy sections are collected in each expansion microscopy experiment. Approximately 20 minutes elapse from when the last expansion tissue is mounted and coverslipped to when the microscope is started. This time includes travelling from the building where the expansion microscopy protocol occurs to a different building where the epifluorescence microscope is located, along with the time it takes to start the microscope and computer.

In contrast to IHC, gelation and digestion control sections, it is more challenging to locate signal and to focus expansion microscopy tissue. In the initial expansion experiments, the process of signal localization and subsequent tissue focusing lasted approximately 30 minutes. Currently this process is roughly 10-15 minutes long. Each expansion microscopy section must be focused as even small differences in tissue thickness can shift the microscope focus location compared to the previous section. Small changes in the fine adjustment knob of a microscope are required to focus expansion microscopy tissue. Consequently, it may take up to 2 hours from the final mounting time to image the last expansion microscopy section. It is possible that the calculated expansion factor for both adult and juvenile LSO cells is less than 10-fold if the collected data pertains to an expansion microscopy section that was imaged at or near the end of an imaging session.

If shrinkage does occur, one solution could be to mount and image a single expansion microscopy section at a time, while keeping the rest of the expansion microscopy sections in ddH_2O. Once the first section is imaged, a new section can be removed from a petri dish containing ddH_2O, mounted and imaged. This process can be repeated until all expansion microscopy sections are imaged to prevent potential expansion shrinkage.

Brainstem Tissue May Reach a Maximum Expansion Factor Less Than X10

Another possible explanation for a less than 10-fold expansion factor in both adult and juvenile LSO cells could be that SOC tissue cannot expand by a factor of 10 using the optimized X10 expansion microscopy protocol. A similar occurrence was observed in the original X10 expansion microscopy publication. Although an expansion factor greater than 10-fold was calculated for COS7 cells and for cultured hippocampal neurons, the expansion factor for rat cerebellum was 9.6-fold (Truckenbrodt et al., 2018).

Variations in the width and length expansion factors for adult and juvenile LSO cells may be explained by the small sample size. Albeit sections for each experiment were collected from the same brain and underwent the same IHC and expansion microscopy protocols, it was not possible to compare the width and length of individual cells prior to expansion microscopy and after expansion. The IHC, gelation, and digestion controls were imaged in order, with expansion microscopy tissue imaged last. Differences between sections and potential expansion shrinkage may account for the measured differences in the width and length expansion factors.

Background Noise in Expansion Microscopy Tissue

Bright puncta are present in multiple expansion microscopy images (Figs. 4,5,6,7). Although not observable in either the IHC, gelation, or digestion controls, it is believed that the bright puncta could be caused by dust particles that fall onto the expansion microscopy tissue or that are already present on the coverslip. Alternatively, the bright puncta could be a result of cleaved secondary antibodies caused by the activity of the proteinase K in the digestion step of the expansion microscopy protocol. The location of the cleaved fluorophores can change from their initial location in the expansion process, resulting in the stochastic bright puncta.

Sources of Resolution Improvement

For the protocol development reported here, most data were collected on an epifluorescence microscope, using a 20X air objective due to the thickness of the expanded tissue. Higher resolution will be achievable using an objective with high numerical aperture. As expected, data collected with the 20X air objective (Figs. 5 and 6) are dimmer than those collected with the 20X oil objective (Fig. 3). An appropriate system for imaging thick, expanded tissue at the inverted confocal microscope, or other microscope, may be necessary.

Expression of VIAAT and VGLUT3

Based on the data shown here, we cannot determine whether specific vesicle proteins are co-expressed on the same synaptic vesicle. In Figure 7, showing contains data collected on a confocal microscope at Nyquist sampling, VGLUT3 and VIAAT immunoreactivity do not appear to be in proximity to each other. However, my preliminary data are not sufficient to answer questions about vesicle populations in the immature LSO. To date, we have shown, using

conventional indirect immunolabeling, that our expansion protocol preserves neighbour-to-neighbour relationships, that our fluorophores survive the expansion process, and that we can expand the tissue by a factor of 10. Conventional indirect immunolabeling methods present two significant disadvantages for our original question: linkage error, and amplification. In order to overcome these disadvantages, singly-conjugated nanobodies should be used with this protocol. The additional use of SIM or SRRF may aid in achieving the resolution required to answer this question.

Expression of Synaptotagmins 1 and 2

Similar questions and caveats apply to the expression of the vesicular transporters and to the calcium sensors. All primary antibodies are well-characterized, and their staining patterns at the resolution of conventional light microscopy are well-established. As with the vesicular transporters, X10 microscopy for the synaptotagmins will require singly-conjugated nanobodies (or direct conjugation of the primary antibodies) to answer the question posed at the outset.

Acknowledgements

The mAb 48 monoclonal antibody developed by Dr. Louis Reichardt at the University of California, San Francisco, was obtained from the Developmental Studies Hybridoma Bank, created by the NICHD of the NIH and maintained at The University of Iowa, Department of Biology, Iowa City, IA 52242. The Zebrafish International Resources Center was used to obtain the znp-1 antibody.

Appendix

Optimized X10 Expansion Microscopy Bench Protocol

Prior Expansion Microscopy Preparation:

- After the anchoring incubation step, wrap the well plate containing micro-dissected LSO nuclei in aluminum foil or cover the well plate with a dark box to minimize fluorophore photobleaching.
- Use serological pipettes for all steps of the expansion microscopy protocol, unless stated otherwise.
- Place two adjacent strips of magic tape approximately 4-5 mm apart on an unsubbed slide. A plastic card can be used to flatten the magic tape onto the slides. It is important that the magic tape is completely flat.
- Create humidified chambers by wrapping the top and bottom of a plastic petri dish with aluminum foil. Humidified chambers can be reused in future expansion microscopy experiments.

Gelation Step

The following steps need to be performed in a fume hood.

1. In a 15 mL conical tube, prepare the monomer gelation solution (MGS) by mixing 2.850 mL of ddH_2O, 0.32g of sodium acrylate, and 1.388 mL DMAA. Vortex the MGS solution until reagents are dissolved.
2. Bubble the MGS solution with N_2 gas for 40 minutes at room temperature.
3. During the 40 minute MGS N_2 bubbling period:
    1. Fold and place a wet (but not dripping) kim wipe on opposite sides of each humidified chamber.
    2. Wash the micro-dissected LSO nuclei twice in 1X PBS at room temperature, for a duration of 5 minutes each. Keep the well plate covered to minimize fluorophore photobleaching.
    3. Fill a container with ice and add just enough cold water to cover the ice.
4. Before the 40 minute MGS solution N_2 bubbling period is complete, add 0.18 g of KPS to 5.0 mL of ddH_2O in a 15 mL conical tube to create the KPS solution and vortex until reagents are dissolved.
5. After the 40 minute MGS solution N_2 bubbling period, transfer 2.7 mL of the MGS solution and 0.3 mL of the KPS solution into a new 15 mL conical tube.
6. Quickly vortex the MGS + KPS solution and place the conical tube in the ice water container.
7. Immediately bubble the MGS + KPS solution with N_2 gas for 15 minutes.
8. During the 15 minute MGS + KPS N_2 bubbling period:
    1. Place a drop of PBS onto each slide and mount the micro-dissected tissue between the strips of magic tape. Remove the PBS around the micro-dissected tissue but do not let the tissue dry out.
    2. Place a staggered coverslip on top of the magic tape to create the gelation chamber.

9. After the 15 minute MGS + KPS N_2 bubbling period, transfer 500 µL of the MGS + KPS solution into a new 1.5 mL Eppendorf tube using a micropipettor. Add 2 µL of TEMED using a micropipettor and quickly vortex the Eppendorf tube to create the polymerizing gelation solution.
10. Immediately transfer the polymerizing gelation solution from the Eppendorf tube to each gelation chamber using a micropipettor. Add just enough polymerizing gelation solution between the coverslip and the slide to fully cover the inside of a gelation chamber (approximately 40-50 µL per slide).
11. Incubate each gelation chamber into an individual humidified chamber for 3 hours at room temperature.

Digestion Step

1. Add proteinase K to the digestion buffer to a dilution of 8 units/mL to create the digestion solution. Vortex the digestion solution.
2. Add the digestion solution to a clean well plate using a micropipettor. Approximately 600 µL of digestion solution per well of a 24-well plate is adequate for micro-dissected LSO nuclei.
3. Use a razor blade to pry open each gelation chamber. Cut the gel that contains tissue with the razor blade and place a drop of digestion buffer solution on the slide to help soften the gel.
4. Carefully remove the tissue-containing gel from the slide with a paintbrush and add the gel to a well containing the digestion solution. One to two tissue-containing gels per well of a 24-well plate is adequate for micro-dissected LSO nuclei.
5. Wrap a wet piece of kim wipe on the closed well plate and then wrap the well plate tightly with aluminum foil.
6. Incubate samples in the digestion solution for 6 hours at 50º C.

Expansion Step

1. After the digestion solution incubation period, remove the aluminum foil and kim wipe from the well plate.
2. Transfer a single gel from the well plate into a petri dish and fill the petri dish with ddH_2O.
3. Repeat step 2 until all gels are transferred.
4. Allow each gel to expand in ddH_2O for approximately 20 minutes.
5. Carefully remove the ddH_2O from each petri dish using a transfer pipette and add new ddH_2O to each petri dish.
6. Repeat step 5 until no further expansion is observed (approximately four ddH_2O washes).
7. Carefully transfer the expanded gel onto a slide using either a paintbrush or by slowly pushing the gel from the petri dish onto the slide.
8. Use a paintbrush to flatten the expanded gel and to remove gel folds. Add a coverslip to the slide without any mounting medium.

Table 1: Validated primary antibodies and antibody concentrations for the optimized X10 expansion microscopy protocol.

Antigen	Host	Concentration	Vendor and Catalogue Number	Antibody Characterization
Syt2	Mouse (monoclonal)	[1:200]	Zebrafish International Resource Center	(Fox & Sanes, 2007) Immunoblot recognized a 60 kDa protein in mouse preparation
VGLUT3	Guinea Pig (polyclonal)	[1:1000]	Synaptic Systems 135204	Preabsoprtion analysis: Antigen aa 543 – 601 of mouse VGLUT 3 (Synaptic Systems) (Fasano et al., 2017) KO verified in VGLUT3-null mice
VIAAT	Rabbit (polyclonal)	[1:1000]	Synaptic Systems 131002	(Takamori et al., 2000) Immunoblot recognized a double band of 57 and 50 kDa Manufacturer Datasheet: KO verified
Syt1	Mouse (monoclonal)	[1:100]	Developmental Studies Hybridoma Bank mAb 48	(Matthew et al., 1981) Immunoblot recognized a 65 kDa protein

Table 2: Validated secondary antibodies and antibody concentrations for the optimized X10 expansion microscopy protocol.

Conjugate	Host	Target	Concentration	Vendor and Catalogue Number
Alexa Fluor 488	Donkey	Mouse	[1:100]	Jackson ImmunoResearch 715-545-151
Alexa Fluor 488	Donkey	Guinea Pig	[1:100]	Jackson ImmunoResearch 705-545-148
Atto 647N	Goat	Rabbit	[1:100]	Rockland 611156122

Table 3: Digestion buffer recipe based on the original X10 expansion microscopy protocol by Truckenbrodt et al., 2018. Proteinase K is not included in the stock solution as is in the original X10 expansion microscopy protocol. Digestion buffer solution was made in ddH_2O and adjusted to pH 8.0 with HCl.

Component	Amount	Vendor and Catalogue Number
Tris Buffer	50 mM	Fisher Scientific BP152-500
Guanidinium chloride	0.8 M	EMD Millipore Corporation 1.04219.0100
Triton X-100	0.5%	Fisher Scientific BP151
Calcium Chloride	2 mM	Fisher Scientific BP510-500

Table 4: List of primary antibody titrations with corresponding vendor/catalogue number and respective notes.

Antigen	Host	Titration	Vendor and Catalogue Number	Notes
Syt2	Mouse	[1:100] [1:200] [1:500]	Zebrafish International Resource Center	[1:200] optimal signal-noise concentration
Syt1	Mouse	[1:50] [1:100] [1:200]	Developmental Studies Hybridoma Bank mAb 48	[1:100] optimal signal-noise concentration
VIAAT	Rabbit	[1:500] [1:1000] [1:2000]	Synaptic Systems 131002	[1:1000] optimal signal-noise concentration
VGLUT3	Guinea Pig	[1:500] [1:1000] [1:2000]	Synaptic Systems 135204	[1:1000] optimal signal-noise concentration

Table 5: List of secondary antibody titrations with corresponding vendor/catalogue number and respective notes.

Conjugate	Host	Target	Titration	Vendor and Catalogue Number	Notes
CF 568	Donkey	Mouse	[1:250] [1:500] [1:1000]	Biotium 20105	[1:250] optimal signal-noise concentration
Atto 488	Goat	Mouse	[1:125] [1:250] [1:500]	Rockland 610-152-121	[1:125] optimal signal-noise concentration
Atto 647N	Goat	Rabbit	[1:125] [1:250] [1:500]	Rockland 611-156-122	[1:125] optimal signal-noise concentration
Alexa Fluor 488	Donkey	Guinea Pig	[1:500]	Jackson ImmunoResearch 706-545-148	Inferior signalling to Alexa Fluor 488 donkey x mouse
Alexa Fluor 647	Donkey	Guinea Pig	[1:500]	Jackson ImmunoResearch 706-605-148	High fluorophore photobleaching

Table 6: List of X10 Expansion Microscopy Reagents.

Reagent	Vendor	Catalog Number
Potassium Persulfate	Sigma-Aldrich	216224
N,N,N',N'-Tetramethylethylenediamine	Sigma-Aldrich	T22500
N,N-Dimethylacrylamide	Sigma-Aldrich	274135
Sodium Acrylate	Sigma-Aldrich	408220
Proteinase K	Sigma-Aldrich	P4850

Table 7: Comparison of original X10 expansion microscopy protocol parameters to the optimized X10 expansion microscopy protocol parameters.

	Original X10 Expansion Microscopy Protocol	Optimized X10 Expansion Microscopy Protocol
Anchoring Duration	At least 6 hours	24 hours
Anchoring Acryloyl-X Concentration	0.1 mg/mL	0.2 mg/mL
Gelation Duration	6-24 hours	3 hours
Digestion Duration	At least 12 hours	6 hours

X10 Expansion Microscopy Troubleshooting

Tissue Sectioning

For a 50 µm section, an expansion factor of 10-fold would in theory increase the thickness of the section to 500 µm. To obtain a greater amount of LSO nuclei, sections at a thickness of 20 µm, 25 µm and 30 µm were tested with the X10 expansion microscopy protocol. Micro-dissected LSO nuclei at 20 µm and 25 µm thickness were too difficult to handle throughout the protocol. At this size, LSO nuclei were harder to micro-dissect and to transfer into the anchoring solution. It was also challenging to transfer the tissue onto each gelation chamber. Furthermore, multiple LSO nuclei were lost during the 1X PBS wash steps. An

adequate section thickness was determined to be 30 µm, as micro-dissected LSO nuclei were easier to handle throughout the expansion microscopy protocol at this size.

LSO Micro-dissection

Two main complications arise when using a full tissue section for X10 expansion microscopy. First, a 10-fold increase in the size of a brainstem section is too large to fit on a microscope slide. Second, the use of proteinase K in the digestion step of the protocol renders the tissue transparent. Consequently, the localization of the LSO nucleus with respect to other surrounding nuclei is not possible. To solve both issues, a scalpel blade is used to micro-dissect the LSO nucleus using a stereo microscope and an external light source. First, water is added on top of a black plastic board, and a petri dish is placed on top of the water to create a 'dark field' viewing setup. Second, 1X PBS is added to the petri dish along with a single IHC section. The distinct shape of the LSO nucleus (Fig. 8) is observed by contrasting the nucleus in relation to the surrounding tissue with the aid of the external light source. Using a scalpel blade, the LSO nucleus is cut from the surrounding tissue and transferred into a well plate with the use of a repurposed tungsten electrode.

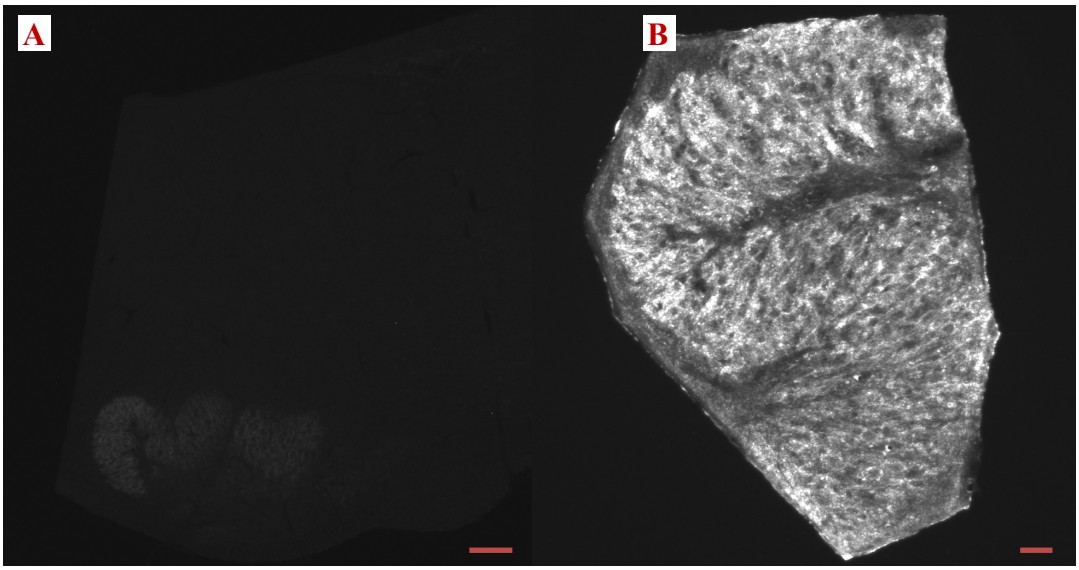

Figure 8: Raw data of P11 SOC (A) and LSO nucleus (B) stained for VGLUT3 and visualized with Alexa Fluor 488. The SOC was imaged with a 2X air objective (0.06 NA) and the micro-dissected LSO was imaged with a 10X air objective (0.25 NA). Scale Bars: (A) 400 µm; (B) 80 µm.

Anchoring Step

Due to the high density of brainstem tissue, both the anchoring duration time and the concentration of the Acryloyl-X solution were modified compared to the original X10 expansion microscopy protocol (Truckenbrodt et al., 2018). First, the anchoring incubation was tested for an 8 hour and a 24 hour incubation time, using sections from a single brain in a solution containing 0.1 mg/mL Acryloyl-X in 1X PBS. No observable differences were seen between the two groups (Fig. 9). Secondly, sections from a single brain were incubated in a solution containing either 0.1, 0.2, or 0.3 mg/mL Acryloyl-X in 1X PBS. Increased signal retention was observed in both the 0.2 and 0.3 mg/mL Acryloyl-X groups (Fig. 10). The 0.3 mg/mL Acryloyl-X concentration produced gels with a shriveled appearance and gels were more difficult to handle during the expansion microscopy protocol.

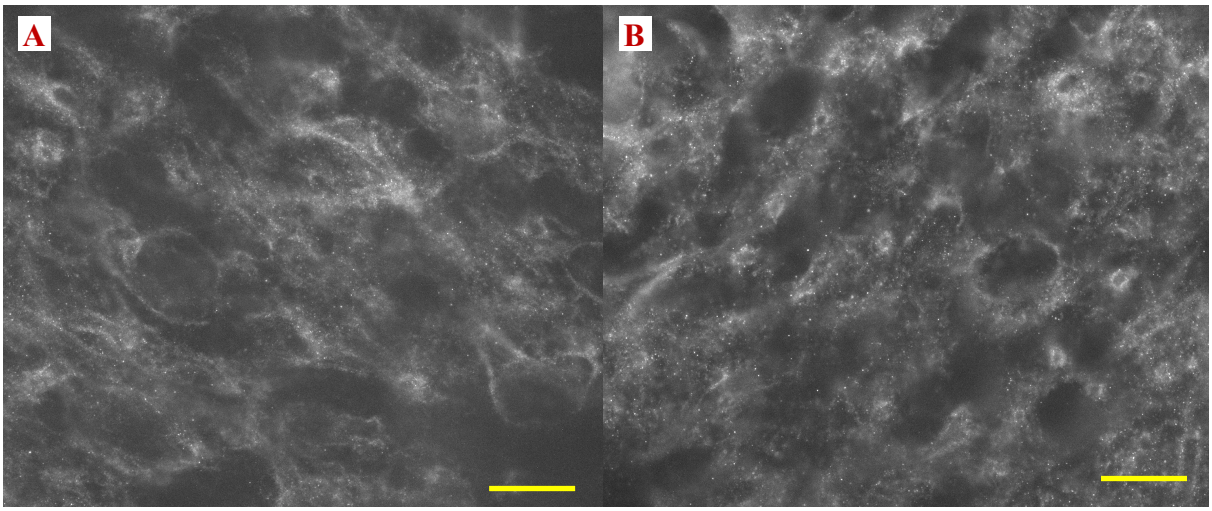

Figure 9: Raw data of P10 LSO lateral limb digestion control cells after 8 hour (A) and 24 hours (B) anchoring incubation times. Images were collected using a 20X air objective (0.45 NA) with the same camera gain and exposure time. Estimated scale bar: 100 µm.

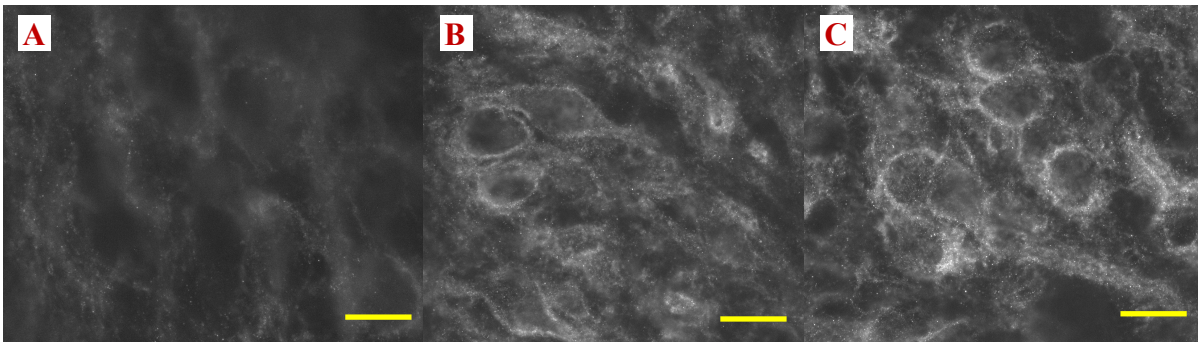

Figure 10: Raw data of LSO middle limb digestion control cells incubated in 0.1 mg/mL (A), 0.2 mg/mL (B), and 0.3 mg/mL (C) Acryloyl-X anchoring solutions. Images were collected using a 20X air objective (0.45 NA) with the same camera gain and exposure time. Estimated scale bar: 100 µm.

Gelation Step

A fire polished Pasteur pipette with a narrow tip diameter is recommended for the 1X PBS wash step to prevent the unwanted suctioning of micro-dissected LSO nuclei into the pipette. Alternatively, micro-dissected LSO nuclei can be transferred into a new well containing 1X PBS between washes with a thin paintbrush. A fine metal wire (e.g., tungsten electrode) can be used to transfer a micro-dissected LSO (Fig. 11) from the well-plate onto the gelation chamber. From experience, a tungsten electrode provided the greatest motility control to transfer

micro-dissected LSO onto a gelation chamber. A thin paintbrush can be used to mount each micro-dissected LSO in a vertical orientation, approximately 2-3 mm apart from each other. The back of a gelation chamber can be marked with a black marker to locate micro-dissected LSO nuclei after completion of the gelation step (Fig. 12).

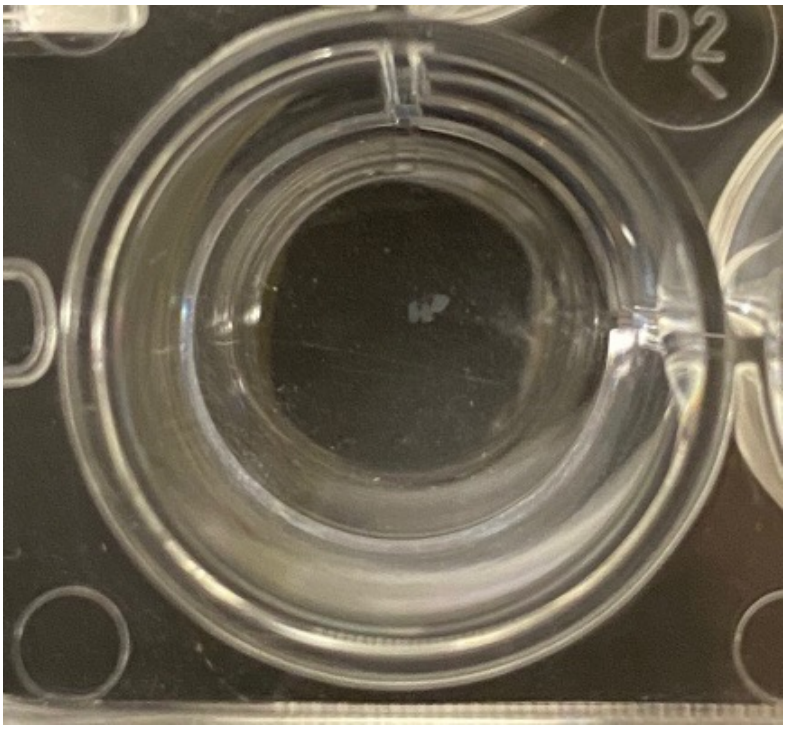

Figure 11: Example of three micro-dissected LSO nuclei in a 24-well plate well.

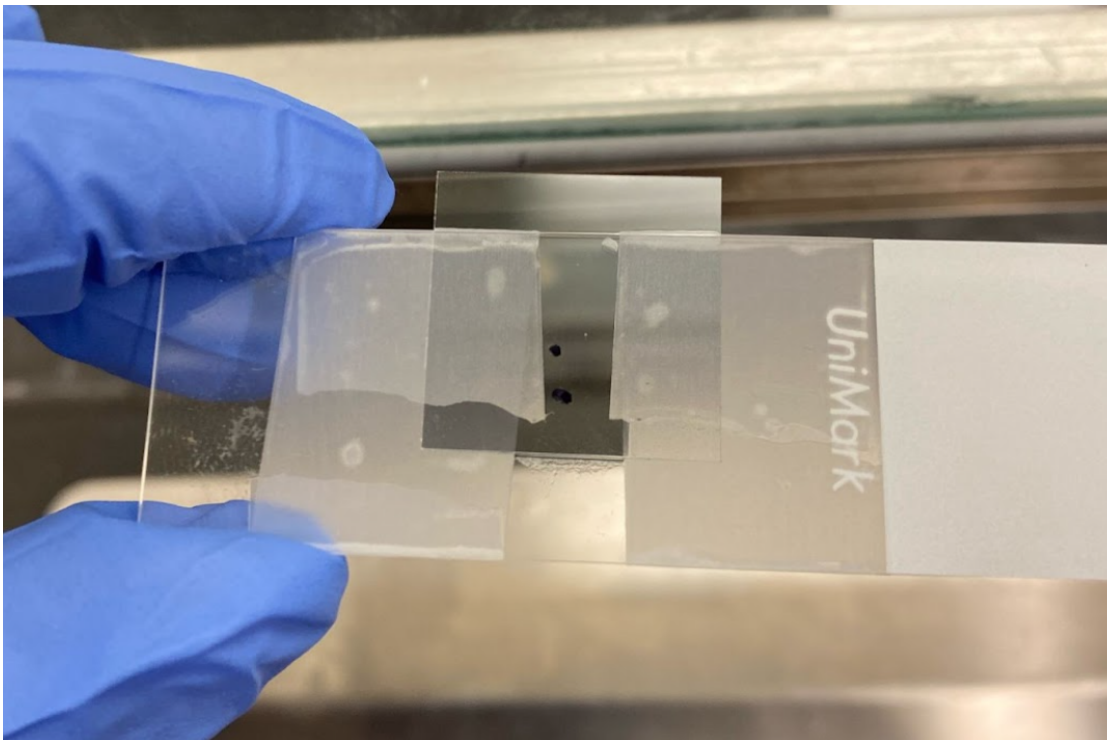

Figure 12: Example of a gelation chamber containing two micro-dissected LSO nuclei. Each black marker dot represents the location of an individual micro-dissected LSO nucleus.

Digestion Step

A razor blade is recommended to carefully pry open each gelation chamber. Hold a razor blade at approximately a 10º angle to a gelation chamber and slowly move the razor blade between the coverslip and slide. Cut the gel from one side of the slide until approximately 2-3 mm from the mounted micro-dissected nuclei. Repeat the process on the other side of the slide. Afterwards, slowly lift the coverslip from one side with the razor blade. Once the coverslip is removed, cut the gel adjacent to the magic tape and slowly remove the magic tape to have easier access to the gel. An external light source can be used to locate the micro-dissected LSO in the gel. Cut each tissue containing gel at a size approximately two-fold the size of each micro-dissected LSO. From experience, gels of smaller dimensions are too difficult to transfer and locate during the expansion process. Once a gel is cut, add a drop of buffer solution to the gel via a transfer pipette and wait approximately 10 seconds before slowly lifting the gel. Use a razor

blade to cut any gel that may reattach to the surrounding gel. Slowly lift the tissue-containing gel using a paintbrush and add the gel into a well plate containing digestion solution. Cover the well plate to minimize light exposure and repeat the previous steps for all micro-dissected LSO nuclei. It is best to keep gels in humidified chambers (Fig. 15) prior to gel cutting to prevent excessive gel hardening. At times, a gel may remain attached to the coverslip when opening a gelation chamber. Albeit more difficult, tissue-containing gel can be removed from a coverslip by following the same procedure as with on-slide gel. Greater attentiveness is needed as a coverslip is more brittle than a slide. Keep one tissue-containing gel as a gelation control and mount the gel on a slide using fluoromount mounting medium.

Expansion Step

A gel may remain adhered to the paintbrush when transferring a digested gel from the well-plate into a petri dish. A transfer pipette can be used to slowly add ddH_2O on top of the gel to move the gel away from the paintbrush and into the petri dish. Micro-dissected LSO nuclei are rendered transparent after the digestion incubation step (Fig. 13). Consequently, an expanding gel has virtually the same transparency as the surrounding ddH_2O in a petri dish. During each ddH_2O removal step, an external light source and a paintbrush can be used to locate where a gel is in a petri dish by observing contrast changes at the gel-ddH_2O boundary. The robustness of a gel diminishes during the expansion process. A paintbrush can be used when removing ddH_2O to slowly hold the gel on one side of a petri dish. From experience, a transfer pipette with a larger diameter opening is best to slowly remove the ddH_2O and transfer into a liquid waste container. Figure 15 displays a fully expanded micro-dissected LSO gel after the removal of ddH_2O. Due to the fragility of a fully expanded gel, it is advised to expand a single gel in an individual petri dish. A wide paint brush can be used to transfer a fully expanded gel onto a slide. However, a

fully expanded gel may rip during this process. Since each micro-dissected LSO is in the middle of a gel, a razor blade can be used to trim away gel from the outer edges and decrease the size of the expanded gel. Alternatively, after the final ddH_2O removal step, a petri dish can be tilted approximately 90º and a fully expanded gel can be slowly moved with a paintbrush onto a slide. Keep one digested gel as a digestion control and mount the gel on a slide using fluoromount mounting medium.

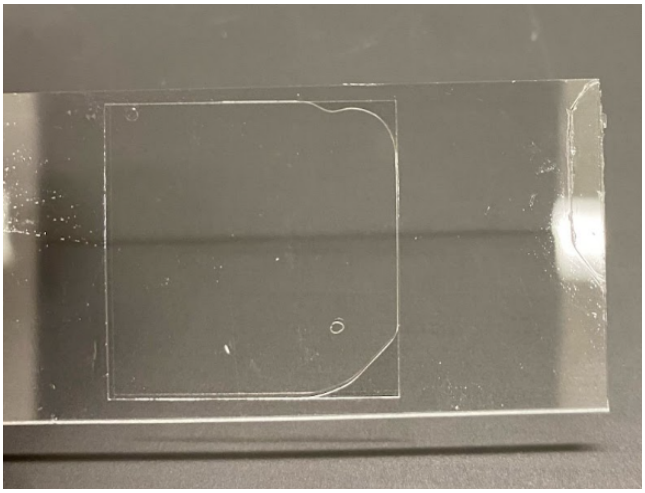

Figure 13: Example of a digestion control gel mounted on a slide with fluoromount mounting medium. Digestion incubation step renders the tissue transparent and indistinguishable from the surrounding gel.

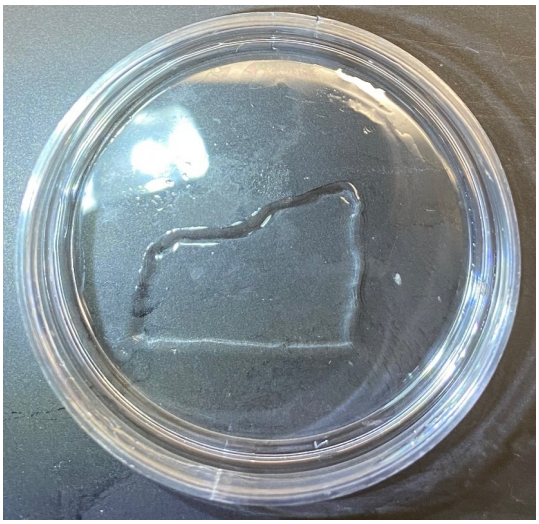

Figure 14: Example of a fully expanded LSO gel in a petri dish after the removal of ddH_2O.

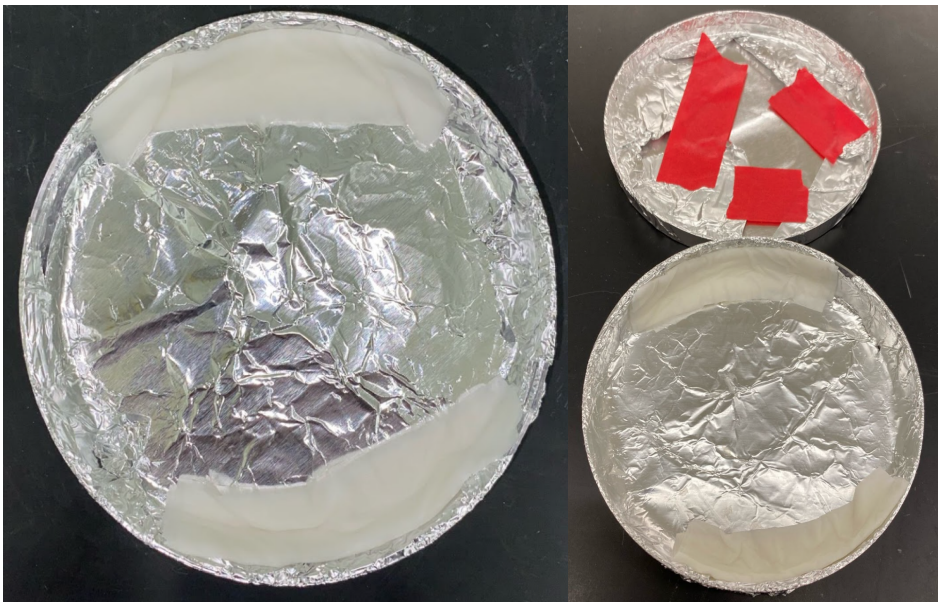

Figure 15: Example of a humidified chamber setup.

Figure 16: Example of N_2 gas bubbling setup.

References

Abbe, E. (1873). Beiträge zur Theorie des Mikroskops und der mikroskopischen Wahrnehmung. *Archiv für Mikroskopische Anatomie*, *9*(1), 413–468.

Aihara, Y., Mashima, H., Onda, H., Hisano, S., Kasuya, H., Hori, T., Yamada, S., Tomura, H., Yamada, Y., Inoue, I., Kojima, I., & Takeda, J. (2000). Molecular cloning of a novel brain-type Na(+)-dependent inorganic phosphate cotransporter. *Journal of Neurochemistry*, *74*(6), 2622–2625.

Alamilla, J., & Gillespie, D. C. (2011). Glutamatergic inputs and glutamate-releasing immature inhibitory inputs activate a shared postsynaptic receptor population in lateral superior olive. *Neuroscience*, *196*, 285–296.

Alamilla, J., & Gillespie, D. C. (2013). Maturation of Calcium-Dependent GABA, Glycine, and Glutamate Release in the Glycinergic MNTB-LSO Pathway. *PLOS ONE*, *8*(9), e75688.

Bellocchio, E. E., Reimer, R. J., Fremeau, R. T., & Edwards, R. H. (2000). Uptake of glutamate into synaptic vesicles by an inorganic phosphate transporter. *Science (New York, N.Y.)*, *289*(5481), 957–960.

Betzig, E., Patterson, G. H., Sougrat, R., Lindwasser, O. W., Olenych, S., Bonifacino, J. S., Davidson, M. W., Lippincott-Schwartz, J., & Hess, H. F. (2006). Imaging intracellular fluorescent proteins at nanometer resolution. *Science (New York, N.Y.)*, *313*(5793), 1642–1645.

Blaesse, P., Ehrhardt, S., Friauf, E., & Nothwang, H. (2005). Developmental pattern of three vesicular glutamate transporters in the rat superior olivary complex. *Cell and Tissue Research*, *320*, 33–50.

Bledsoe, S. C., Snead, C. R., Helfert, R. H., Prasad, V., Wenthold, R. J., & Altschuler, R. A. (1990). Immunocytochemical and lesion studies support the hypothesis that the projection from the medial nucleus of the trapezoid body to the lateral superior olive is glycinergic. *Brain Research*, *517*(1–2), 189–194.

Boudreau, J. C., & Tsuchitani, C. (1968). Binaural interaction in the cat superior olive S segment. *Journal of Neurophysiology*, *31*(3), 442–454.

Cant, N. B., & Casseday, J. H. (1986). Projections from the anteroventral cochlear nucleus to the lateral and medial superior olivary nuclei. *The Journal of Comparative Neurology*, *247*(4), 457–476.

Case, D. T., & Gillespie, D. C. (2011). Pre- and postsynaptic properties of glutamatergic transmission in the immature inhibitory MNTB-LSO pathway. *Journal of Neurophysiology*, *106*(5), 2570–2579.

Case, D. T., Zhao, X., & Gillespie, D. C. (2011). Functional Refinement in the Projection from Ventral Cochlear Nucleus to Lateral Superior Olive Precedes Hearing Onset in Rat. *PLOS ONE*, *6*(6), e20756.

Chaudhry, F. A., Reimer, R. J., Bellocchio, E. E., Danbolt, N. C., Osen, K. K., Edwards, R. H., & Storm-Mathisen, J. (1998). The vesicular GABA transporter, VGAT, localizes to synaptic vesicles in sets of glycinergic as well as GABAergic neurons. *The Journal of Neuroscience: The Official Journal of the Society for Neuroscience*, *18*(23), 9733–9750.

Chen, F., Tillberg, P. W., & Boyden, E. S. (2015). Expansion Microscopy. *Science (New York, N.Y.)*, *347*(6221), 543–548.

Cooper, A. P., & Gillespie, D. C. (2011). Synaptotagmins I and II in the developing rat auditory brainstem: Synaptotagmin I is transiently expressed in glutamate-releasing immature inhibitory terminals. *Journal of Comparative Neurology*, *519*(12), 2417–2433.

Dumoulin, A., Rostaing, P., Bedet, C., Lévi, S., Isambert, M. F., Henry, J. P., Triller, A., & Gasnier, B. (1999). Presence of the vesicular inhibitory amino acid transporter in GABAergic and glycinergic synaptic terminal boutons. *Journal of Cell Science*, *112 (Pt 6)*, 811–823.

Ehrlich, I., Löhrke, S., & Friauf, E. (1999). Shift from depolarizing to hyperpolarizing glycine action in rat auditory neurones is due to age-dependent Cl− regulation. *The Journal of Physiology*, *520*(Pt 1), 121–137.

Fasano, C., Rocchetti, J., Pietrajtis, K., Zander, J.-F., Manseau, F., Sakae, D. Y., Marcus-Sells, M., Ramet, L., Morel, L. J., Carrel, D., Dumas, S., Bolte, S., Bernard, V., Vigneault, E., Goutagny, R., Ahnert-Hilger, G., Giros, B., Daumas, S., Williams, S., & El Mestikawy, S. (2017). Regulation of the Hippocampal Network by VGLUT3-Positive CCK-GABAergic Basket Cells. *Frontiers in Cellular Neuroscience*, *11*.

Fox, M. A., & Sanes, J. R. (2007). Synaptotagmin I and II are present in distinct subsets of central synapses. *The Journal of Comparative Neurology*, *503*(2), 280–296.

Fremeau, R. T., Burman, J., Qureshi, T., Tran, C. H., Proctor, J., Johnson, J., Zhang, H., Sulzer, D., Copenhagen, D. R., Storm-Mathisen, J., Reimer, R. J., Chaudhry, F. A., & Edwards, R. H. (2002). The identification of vesicular glutamate transporter 3 suggests novel modes of signaling by glutamate. *Proceedings of the National Academy of Sciences*, *99*(22), 14488–14493.

Fremeau, R. T., Troyer, M. D., Pahner, I., Nygaard, G. O., Tran, C. H., Reimer, R. J., Bellocchio, E. E., Fortin, D., Storm-Mathisen, J., & Edwards, R. H. (2001). The expression of vesicular glutamate transporters defines two classes of excitatory synapse. *Neuron*, *31*(2), 247–260.

Gillespie, D. C., Kim, G., & Kandler, K. (2005). Inhibitory synapses in the developing auditory system are glutamatergic. *Nature Neuroscience*, *8*(3), 332–338.

Goldberg, J. M., & Brown, P. B. (1968). Functional organization of the dog superior olivary complex: An anatomical and electrophysiological study. *Journal of Neurophysiology*, *31*(4), 639–656.

Gras, C., Herzog, E., Bellenchi, G. C., Bernard, V., Ravassard, P., Pohl, M., Gasnier, B., Giros, B., & El Mestikawy, S. (2002). A Third Vesicular Glutamate Transporter Expressed by Cholinergic and Serotoninergic Neurons. *The Journal of Neuroscience*, *22*(13), 5442–5451.

Gustafsson, M. G. L. (2000). Surpassing the lateral resolution limit by a factor of two using structured illumination microscopy. *Journal of Microscopy*, *198*(2), 82–87.

Gustafsson, N., Culley, S., Ashdown, G., Owen, D. M., Pereira, P. M., & Henriques, R. (2016). Fast live-cell conventional fluorophore nanoscopy with ImageJ through super-resolution radial fluctuations. *Nature Communications*, *7*(1), 12471.

Harris, K. M., & Sultan, P. (1995). Variation in the number, location and size of synaptic vesicles provides an anatomical basis for the nonuniform probability of release at hippocampal CA1 synapses. *Neuropharmacology*, *34*(11), 1387–1395.

Heintzmann, R., & Cremer, C. (1999). Laterally modulated excitation microscopy: Improvement of resolution by using a diffraction grating. *Proc. SPIE*, *3568*, 185–196.

Hell, S. W., & Kroug, M. (1995). Ground-state-depletion fluorscence microscopy: A concept for breaking the diffraction resolution limit. *Applied Physics B*, *60*(5), 495–497.

Hell, S. W., & Wichmann, J. (1994). Breaking the diffraction resolution limit by stimulated emission: Stimulated-emission-depletion fluorescence microscopy. *Optics Letters*, *19*(11), 780–782.

Hess, S. T., Girirajan, T. P. K., & Mason, M. D. (2006). Ultra-High Resolution Imaging by Fluorescence Photoactivation Localization Microscopy. *Biophysical Journal*, *91*(11), 4258–4272.

Kandler, K., & Friauf, E. (1995). Development of glycinergic and glutamatergic synaptic transmission in the auditory brainstem of perinatal rats. *Journal of Neuroscience*, *15*(10), 6890–6904.

Kim, G., & Kandler, K. (2003). Elimination and strengthening of glycinergic/GABAergic connections during tonotopic map formation. *Nature Neuroscience*, *6*(3), 282–290.

Klar, T. A., Jakobs, S., Dyba, M., Egner, A., & Hell, S. W. (2000). Fluorescence microscopy with diffraction resolution barrier broken by stimulated emission. *Proceedings of the National Academy of Sciences*, *97*(15), 8206–8210.

Kotak, V. C., Korada, S., Schwartz, I. R., & Sanes, D. H. (1998). A developmental shift from GABAergic to glycinergic transmission in the central auditory system. *The Journal of Neuroscience: The Official Journal of the Society for Neuroscience*, *18*(12), 4646–4655.

Matthew, W. D., Tsavaler, L., & Reichardt, L. F. (1981). Identification of a synaptic vesicle-specific membrane protein with a wide distribution in neuronal and neurosecretory tissue. *Journal of Cell Biology*, *91*(1), 257–269.

McIntire, S. L., Reimer, R. J., Schuske, K., Edwards, R. H., & Jorgensen, E. M. (1997). Identification and characterization of the vesicular GABA transporter. *Nature*, *389*(6653), 870–876.

Nabekura, J., Katsurabayashi, S., Kakazu, Y., Shibata, S., Matsubara, A., Jinno, S., Mizoguchi, Y., Sasaki, A., & Ishibashi, H. (2004). Developmental switch from GABA to glycine release in single central synaptic terminals. *Nature Neuroscience*, *7*(1), 17–23.

Noh, J., Seal, R. P., Garver, J. A., Edwards, R. H., & Kandler, K. (2010). Glutamate co-release at GABA/glycinergic synapses is crucial for the refinement of an inhibitory map. *Nature Neuroscience*, *13*(2), 232–238.

Rayleigh. (1896). XV. On the theory of optical images, with special reference to the microscope. *The London, Edinburgh, and Dublin Philosophical Magazine and Journal of Science*, *42*(255), 167–195.

Rust, M. J., Bates, M., & Zhuang, X. (2006). Stochastic optical reconstruction microscopy (STORM) provides sub-diffraction-limit image resolution. *Nature Methods*, *3*(10), 793–795.

Sagné, C., El Mestikawy, S., Isambert, M. F., Hamon, M., Henry, J. P., Giros, B., & Gasnier, B. (1997). Cloning of a functional vesicular GABA and glycine transporter by screening of genome databases. *FEBS Letters*, *417*(2), 177–183.

Schikorski, T., & Stevens, C. F. (1997). Quantitative ultrastructural analysis of hippocampal excitatory synapses. *The Journal of Neuroscience: The Official Journal of the Society for Neuroscience*, *17*(15), 5858–5867.

Schindelin, J., Arganda-Carreras, I., Frise, E., Kaynig, V., Longair, M., Pietzsch, T., Preibisch, S., Rueden, C., Saalfeld, S., Schmid, B., Tinevez, J.-Y., White, D. J., Hartenstein, V.,

Eliceiri, K., Tomancak, P., & Cardona, A. (2012). Fiji: An open-source platform for biological-image analysis. *Nature Methods*, *9*(7), 676–682.

Sharonov, A., & Hochstrasser, R. M. (2006). Wide-field subdiffraction imaging by accumulated binding of diffusing probes. *Proceedings of the National Academy of Sciences of the United States of America*, *103*(50), 18911–18916.

Takamori, S., Rhee, J. S., Rosenmund, C., & Jahn, R. (2000). Identification of a vesicular glutamate transporter that defines a glutamatergic phenotype in neurons. *Nature*, *407*(6801), 189–194.

Takamori, S., Riedel, D., & Jahn, R. (2000). Immunoisolation of GABA-Specific Synaptic Vesicles Defines a Functionally Distinct Subset of Synaptic Vesicles. *The Journal of Neuroscience*, *20*(13), 4904–4911.

Truckenbrodt, S., Maidorn, M., Crzan, D., Wildhagen, H., Kabatas, S., & Rizzoli, S. O. (2018). X10 expansion microscopy enables 25-nm resolution on conventional microscopes. *EMBO Reports*, *19*(9), e45836.

Wu, S., & Kelly, J. (1992). Synaptic pharmacology of the superior olivary complex studied in mouse brain slice. *The Journal of Neuroscience*, *12*(8), 3084–3097.